J. Fluid Mech. (1996), *vol.* 306, *pp.* 59–82

Instability of a rotating shear layer in the transonic regime

By M. TOMASINI[1], N. DOLEZ[1] AND J. LÉORAT[2]

[1]Observatoire Midi-Pyrénées, 14 Avenue E. Belin, 31400 Toulouse, France
[2]Observatoire de Paris-Meudon, DAEC, Place J. Janssen, 92195 Meudon, France

(Received 10 March 1995 and in revised form 26 August 1995)

We have studied numerically the stability of a two-dimensional Couette flow in a polytropic fluid subjected to a localized shear, using a pseudo-spectral method (Fourier–Chebyshev). The polytropic index has been chosen equal to 2 and a radial force (pseudo-gravity) is introduced in order to perform comparisons with the shallow water experimental results. When the Reynolds number is not too low, the initial flow which is purely azimuthal becomes unstable and a stable rotating pattern is formed, with a number of azimuthal modes which decreases when the Mach number increases. A qualitative agreement is found with the experimental results, although the spatial resolution constraint strongly limits the numerical Reynolds and Mach numbers. From the variation of the linear growth rate of the unstable modes with the Mach number, we are able to show the transition between a flow subjected to Kelvin–Helmholtz instability towards one essentially driven by a centrifugal instability, which is efficient for rotating supersonic flows if the angular momentum decreases outwards. The latter situation may occur for some flows in astrophysical disks.

1. Introduction

Very little is known about the dynamics of rotating flows when compressibility is effective. Besides theoretical motivations, many practical applications require an increased knowledge in this field. Astrophysical disks represent an important class of such flows, where the conservation of angular momentum in a given central gravitational potential leads to the formation of a shear flow in a disk which may be considered as thin. Such a bidimensional flow configuration explains many observations, including the formation of the solar planetary system. Note that we do not intend here to study the dynamics of astrophysical disks, which are supported by gravitation and not by rigid boundaries, may have a radial mean flow and also experience magnetic forces. It is hoped however that astrophysical problems may benefit from numerical and experimental advances for the simpler situation which will be examined below concerning the dynamics of a shear layer in a compressible rotating two-dimensional flow, uniform in the axial direction.

It has been shown analytically that compressibility provides an efficient source of instability with respect to non-axisymmetric perturbations in the case where the angular velocity is a power law of the radius (Goldreich & Lynden-Bell 1965; Papaloizou & Pringle 1984; Narayan, Goldreich & Goodman 1987; Glatzel 1987*(a, b)*).

The case where the shear is concentrated in a narrow radius range provides another theoretically and practically meaningful rotating flow configuration. An astrophysical example of such rotating shear flow may be found in some galaxies where the azimuthal velocity exhibits a narrow peak close to the central nucleus (see for example, Zasov & Zotov 1989). In the limit of negligible curvature, one gets a plane parallel flow subject to the classical Kelvin–Helmholtz instability. In the case of the thin disk approximation, the flow may reach supersonic velocities and the Kelvin–Helmholtz stability criterion is deeply modified by three main effects: compressibility, curvature and boundary conditions (centre and external medium). The stability of this flow configuration may be studied using experimental, linear theory and numerical approaches.

This type of flow has been experimentally investigated by M. Nezlin and his co-workers (for a review, see Nezlin & Snezhkin 1993), exploiting the formal analogy of two-dimensional gas dynamics with a shallow water system. In the dynamical equations, the fluid height H of the incompressible shallow water system is analogous to the fluid density of a polytropic fluid ($\gamma = 2$) while the surface gravity wave speed $(gH)^{1/2}$ corresponds to the sound speed. These experiments make it possible to produce quasi-two-dimensional 'supersonic' flows in a rotating container with a diameter of about 60 centimetres and show the formation of structures under forcing with a localized shear. The source of the instability could be the mixing layer, which is unstable at large scales for an incompressible fluid, as was realized in the experiments of Chomaz *et al.* (1988). It is experimentally verified by Fridman *et al.* (1985) that the supersonic regime is also unstable, and, since the two-dimensional mixing layer is known to become stable in the plane supersonic case (Blumen, Drazin & Billings 1975), another type of instability mechanism is thought to be acting, related to the negative gradient of angular momentum. The stability criterion for a two-dimensional perturbation was first derived by Landau (1944). In the case of shallow water flows, the analogous criterion has been described by Bazdenkov & Pogutse (1983) and experimentally verified by Antipov *et al.* (1983).

The linear stability of the rotating shear layer has been examined by Morozov (1977) and Fridman (1979, 1989) in the inviscid case. In the limit of high radial wavenumbers which correspond to tightly wound spirals, when the angular momentum is radially decreasing, these authors find an instability growth rate proportional to the square of the angular velocity and inversely proportional to the sound velocity. These results show that compressibility is necessary in order for a 'centrifugal instability' to act in two-dimensional flows. Nezlin & Snezhkin (1993) present arguments indicating that the latter mechanism could be responsible for the instability observed in their experiments and also for some observed spiral galaxies. However, the available analytical studies cannot be used directly to describe realistic situations, since some approximations are needed to solve the dispersion equation: viscosity cannot be neglected in experiments and numerical simulations; observed spirals (experimental and astrophysical) are not tightly wound; bottom friction is significant in the experiments, etc.

Prompted by the results of the rotating tank experiments, we have thus performed numerical experiments with parameters as close as possible to the laboratory configuration, in order to study the linear instability of the shear flow and also the formation of structures under the nonlinear interactions.

The paper is organized as follows: the next section gives the general characteristics of the numerical method and the main parameters used to control the flow. Numerical

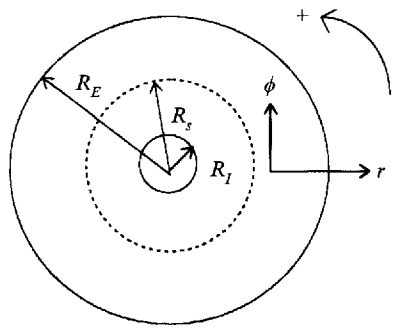

FIGURE 1. Geometrical data. The shear is centred on radius R_s. The cylindrical coordinates are r, ϕ.

results in the nonlinear regime are presented in §3. Section 4 concentrates on the study of the influence of the Mach number on linear instability growth rates to determine the nature of the instabilities and the concluding section gives a preliminary discussion of the relations between the experimental, analytical and numerical results.

2. Numerical method

The numerical code used in our simulation is a bidimensional pseudo-spectral code, written by N. Dolez and J. Léorat. The Navier–Stokes equations are solved in annular geometry, for a compressible, viscous barotropic fluid (the pressure is function of the density only: $P \sim \rho^{\gamma}$).

The domain of simulation is an annulus, with internal and external radii, R_I and R_E as shown in figure 1. To remain as close as possible of the experimental settings, the main geometrical factors are kept constant. In non-dimensional units: $R_I = 0.2$, $R_E = 2.2$ and the radius of strongest shear (shear inflexion point) is $R_s = 0.8$.

We use rigid boundary conditions on the internal and external radii of the annulus, where the angular velocities (Ω_I and Ω_E) are fixed (cf. initial conditions §2.3 below).

2.1. *Equations*

The equations are non-dimensionalized assuming a constant kinematic viscosity, ν. The unit of length is the annulus half-width $(R_E^* - R_I^*)/2$, where the asterisk denotes a dimensional quantity. The speed unit is the tangential velocity at the internal boundary $V_I^* = \Omega_I^* R_I^*$. The pressure P^* is put in dimensionless form with the value of the sound speed c^* calculated with the polytropic hypothesis: $c^{*2} = \gamma P^*/\rho^*$. The density unit is the mean density.

In cylindrical coordinates in a fixed reference frame, the tangential velocity u_ϕ, the radial velocity u_r and the density ρ satisfy

$$\frac{\partial u_\phi}{\partial t} = -u_\phi \frac{\partial u_\phi}{r\partial \phi} - u_r \frac{\partial u_\phi}{\partial r} - \frac{u_\phi u_r}{r} - \frac{\rho^{\gamma-2}}{c^2}\frac{\partial \rho}{r\partial \phi} + F_{v\phi} + F_s + F_f, \tag{2.1}$$

$$\frac{\partial u_r}{\partial t} = -u_\phi \frac{\partial u_r}{r\partial_\phi} - u_r \frac{\partial u_r}{\partial r} + \frac{u_\phi^2}{r} - \frac{\rho^{\gamma-2}}{c^2}\frac{\partial \rho}{\partial r} + F_{vr} + F_r, \tag{2.2}$$

$$\frac{\partial \rho}{\partial t} = -u_\phi \frac{\partial \rho}{r\partial \phi} - u_r \frac{\partial \rho}{\partial r} - \frac{\rho u_r}{r} - \rho \frac{\partial u_\phi}{r\partial \phi} - \rho \frac{\partial u_r}{\partial r}, \tag{2.3}$$

where

$$F_{v\phi} = \frac{v}{r}\left(\frac{\partial(r\sigma_{\phi r})}{\partial r} + \frac{\partial \sigma_{\phi\phi}}{\partial \phi} + \sigma_{\phi r} + \frac{\sigma_{\phi\phi}}{\rho}\frac{\partial \rho}{\partial \phi} + \frac{r\sigma_{\phi r}}{\rho}\frac{\partial \rho}{\partial r}\right),$$

$$F_{vr} = \frac{v}{r}\left(\frac{\partial(r\sigma_{rr})}{\partial r} + \frac{\partial \sigma_{\phi r}}{\partial \phi} - \sigma_{\phi\phi} + \frac{\sigma_{\phi r}}{\rho}\frac{\partial \rho}{\partial \phi} + \frac{r\sigma_{rr}}{\rho}\frac{\partial \rho}{\partial r}\right),$$

with

$$\sigma_{\phi\phi} = 2\left(\frac{\partial u_\phi}{r\partial \phi} + \frac{u_r}{r}\right) - \tfrac{2}{3}\nabla \cdot \boldsymbol{u},$$

$$\sigma_{\phi r} = \frac{\partial u_r}{r\partial \phi} + \frac{\partial u_\phi}{\partial r} - \frac{u_\phi}{r},$$

$$\sigma_{rr} = 2\frac{\partial u_r}{\partial r} - \tfrac{2}{3}\nabla \cdot \boldsymbol{u},$$

where

$$\nabla \cdot \boldsymbol{u} = \frac{1}{r}\frac{\partial(ru_r)}{\partial r} + \frac{1}{r} + \frac{\partial u_\phi}{\partial \phi}$$

for a monoatomic gas. In the runs reported below, $\gamma = 2$ in order to take advantage of the analogy of gas dynamics with experimental shallow water systems.

The different forcing terms F_s, F_f and F_r in the equations are discussed in §2.4.

2.2. *Spatial and temporal integrations*

The equations are discretized using a pseudo-spectral scheme with Fourier transforms in the azimuthal direction, which is periodical, and Chebyshev polynomials in the radial direction, which allows the implementation of the boundary conditions with a tau-collocation method.

Time stepping uses a mixed Adams–Bashforth and Crank–Nicholson scheme: only the second radial derivatives appearing in the diffusion terms needs to be treated implicitly. The reason is that they would impose a constraint on the time step proportional to $1/N^4$ (where N is the number of Chebyshev polynomials retained in the code) if they were treated explicitly. On the other hand, the second derivatives in the Fourier direction impose only a constraint of $1/M^2$ (M is the number of Fourier functions), no worse than the first Chebyshev derivative, which appears in any case in some of the nonlinear terms treated explicitly. The implicit matrix operator is then very simple, and can be reduced to a five-diagonal banded matrix. The boundary conditions are expressed in spectral space, and appears as two additional full lines in the implicit matrix. The direct method, like double sweeping, enables us to solve the system in a number of operations proportional to the spectral resolution N. Most of our simulations have been performed with a resolution of $M \times N = 64 \times 65$ or 64×129 and exceptionally of 128×129 grid points.

2.3. *Initial conditions and shear characteristics*

We choose a basic profile of angular velocity of the form

$$\Omega(r, t = 0) = A \tanh\left[\frac{2(r - R_s)}{e_s}\right] + B, \tag{2.4}$$

where A and B are constants chosen so that Ω satisfies the boundary conditions. Such a profile (curve A of figure 2) represents basically the fitting of two solid rotation

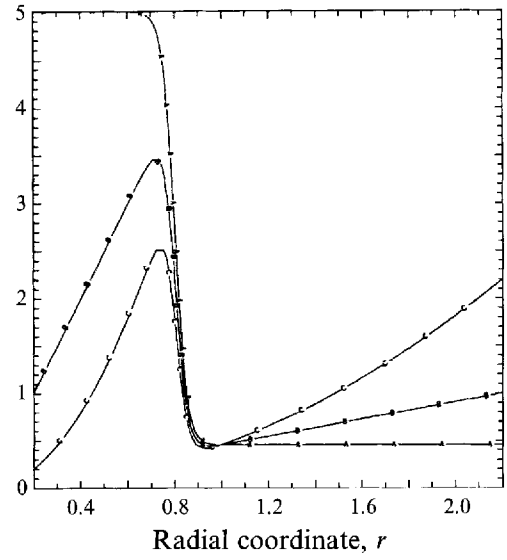

FIGURE 2. Initial unperturbed profiles as a function of the radial coordinate: curve A for angular velocity $\Omega(r, t = 0)$, curve B for azimuthal velocity $V(r) = u_\phi(r, t = 0) = \Omega(r, t = 0)r$, curve C for angular momentum $\Omega(r, t = 0)r^2$. The curves have been plotted for the following parameters: $\Omega_I = 5, \Omega_E = 0.454545, e_s = 0.1, R_I = 0.2, R_s = 0.8, R_E = 2.2, N = 129$.

zones in the annulus, with a hyperbolic tangent transition zone of characteristic width e_s situated at radius R_s. We define the initial tangential velocity as

$$V(r) = u_\phi(r, t = 0) = r\Omega(r, t = 0)$$

which is plotted on figure 2 (curve B).

We superpose a white noise on the basic velocity around the shear for the instability to develop. The perturbed energy per mode varies generally from 1% of the initial basic kinetic energy for the lowest Fourier wavenumbers down to 0.001% for the largest ones.

The initial density is uniform and set to unity.

Let us define three dimensionless characteristic numbers fixed by the initial conditions. The fluid Mach number Ma is equivalent to a convective Mach number†:

$$Ma = \frac{|\Omega_I - \Omega_E| R_s}{2c}. \tag{2.5}$$

Similarly, the Reynolds number Re based on the same characteristic velocity jump and on the shear width is

$$Re = \frac{|\Omega_I - \Omega_E| R_s e_s}{2\nu}. \tag{2.6}$$

Ro is identified with a local Rossby number based on the velocity jump and the shear width:

$$Ro = \frac{\text{nonlinear term}}{\text{rotation term}} = \left| \frac{V \partial V / \partial r}{2\Omega V} \right| \approx \left| \frac{\Omega_I - \Omega_E}{\Omega_I + \Omega_E} \right| \frac{R_s}{e_s}. \tag{2.7}$$

† Our Mach number is two times smaller than the one of Nezlin & Snezhkin (1993).

2.4. *External forces*

Equations (2.1) and (2.2) include several additional external forces which may be used to represent different physical effects; they are very important for comparisons with experiments:

(i) F_r is a radial force ('pseudo-gravity') adjusted to compensate exactly the centrifugal force of the unperturbed velocity profile. The main effect is to assure a uniform density and no pressure gradient in the unperturbed state. A uniform density, in equilibrium with the centripetal and gravity acceleration, corresponds to the experimental conditions of Nezlin *et al.* (1986) (constant depth in the shallow water). F_s and F_f are two different kinds of tangential forces devised to maintain the shear in the flow:

(ii) In most of our simulations, we are interested in keeping a very narrow zone where the shear occurs in the flow: if we want to make some comparisons with the results of Nezlin & Snezhkin (1993) and of Chomaz *et al.* (1988), the width of the shear zone ($\approx e_s$) should be less than one tenth of the radius R_s. Due to a fairly high viscosity (which is imposed by a lack of resolution of our simulations) the shear we impose in the flow initially would be dissipated in a time shorter than, or of the same order as, the characteristic unfolding time of the instabilities. To prevent this artificial widening, we maintain the shear by the force F_s, which compensates the viscous forces generated by the unperturbed profile:

$$F_s = -F_{v\phi}(t=0) = -\nu\left(\frac{\partial^2 V(r)}{\partial r^2} + \frac{\partial V(r)}{r\partial r} - \frac{V(r)}{r^2}\right). \tag{2.8}$$

Note that F_s is constant while $F_{v\phi}$ changes according to the fluid dynamics.

(iii) The third force, F_f, acts as a friction and is proportional to the difference between the actual and the initial azimuthal velocity: we used it especially for comparisons with experiments, where the friction, dominating the viscous force, can play an important role in the dynamics:

$$F_f = -\alpha(u_\phi(r,\phi,t) - V(r)). \tag{2.9}$$

F_f can be considered as a modelization of the viscous terms involving the axial shear of the flow in the experiments. It can be shown (Chomaz *et al.* 1988) that α is proportional to ν/H^2 where H is the thickness of the fluid layer. Note that this friction term has a strong stabilizing effect on the flow. The value of the coefficient is discussed in §3.1.

Our numerical simulations enable us to study the transient flow where the linear instability develops as well as the subsequent quasi-steady flow stabilized by the nonlinear interactions. The latter regime allows a direct comparaison of numerical and experimental results. It will be presented first, while the study of the time-dependent flow instability (linear regime) will be developed in §4.

3. Formation of the stable structures

The shallow water experiments show that a concentrated shearing force in compressible rotating flows leads to the formation of non-axisymmetric spiral-like structures for the density and velocity. The pattern angular velocity, which has the same sign as the mean azimuthal flow, and its geometrical characteristics (spirals number, pitch angle, etc.) are related to the shear profile (controlled by the parameter e_s), to the

e_s	0.8	0.4	0.2	0.06
Re	145.5	72.7	36.4	10.9
Ro	0.8	1.7	3.3	11.1
m_0	1	2	3	3

TABLE 1. Variation of the azimuthal order m of the most energetic mode as a function of the shear width e_s. The following parameters are fixed in the simulations: $1/c = 0.5, Ma = 0.9, 1/v = 100, V_I = V_E = 1, \alpha = 0$ (no friction). The characteristic Reynolds number Re and the Rossby number Ro are given.

mean radius of the shear annulus (R_s) and to the fluid characteristic Mach number Ma.

Note that an analytical determination of the structures characteristics would be a difficult task since this is equivalent to searching for steady solutions of the nonlinear dynamical equations in the non-axisymmetric case. Moreover one must take into account the hysteresis which is encountered in the laboratory as well as in the numerical experiments (cf. Chomaz *et al.* 1988 in the incompressible case, or Nezlin & Snezhkin 1993 for the shallow water results). We thus concentrate here on the numerical approach, which obviously also presents some difficulties in the supersonic and high Reynolds number regimes.

We only consider flows with a shear width as small as possible compared to the shear radius, in the transonic regime ($Ma \approx 1$), and do not intend to study the Rossby regime corresponding to relatively large shear width that dominates rotation in the nonlinear terms ($Ro \ll 1$), which could be simulated using the same numerical code. Marcus (1990) has also numerically studied the stability of a two-dimensional rotating shear layer. Note however that in this computation the fluid is incompressible, inviscid and the Rossby number is small, so that quantitative comparisons are excluded.

3.1. *Choice of the main parameters*

After the initial transient evolution, a steady state is achieved. We have first checked that the azimuthal mode number m_0 is strongly dependent on the shear width e_s, in agreement with the experimental results. Table 1 summarizes some characteristic values, varying only e_s between 0.8 and 0.06 and keeping all other parameters fixed.

The characteristic Reynolds number Re changes because of e_s (cf. equation (2.6)). But the increase in m_0 with decreasing e_s is still obtained if we keep Re constant (for example by increasing $1/v$ with decreasing e_s) because the viscous force damps the high frequencies first.

In the first case ($e_s = 0.8$), one observes an anticyclonic† vortex with an increase of density. The low value of the Rossby number shows that it belongs to the Rossby regime rather than to that of the strong shear we want to examine.

The shear width, the Mach number and the Reynolds number are severely constrained by the available spatial resolution. As stated in the previous section, we try to maintain the smallest shear. The distance Δr between two adjacent grid points at

† By definition, the cyclonic rotation direction is the one of the main flow and is given by the inner annulus. Any rotation in the opposite direction is called anticyclonic. In the Rossby regime, the Coriolis force balances the pressure force (geostrophic equilibrium). The centrifugal force is negligible and the eddies due to this regime are large enough and their proper velocity small enough to be influenced by the global rotation (of a planet for example). Their characteristic life times are several times the rotation period of the planet. The cyclones (rotation vector parallel to the planet one) are characterized by low pressures and the anticyclones by overpressures in the Rossby regime.

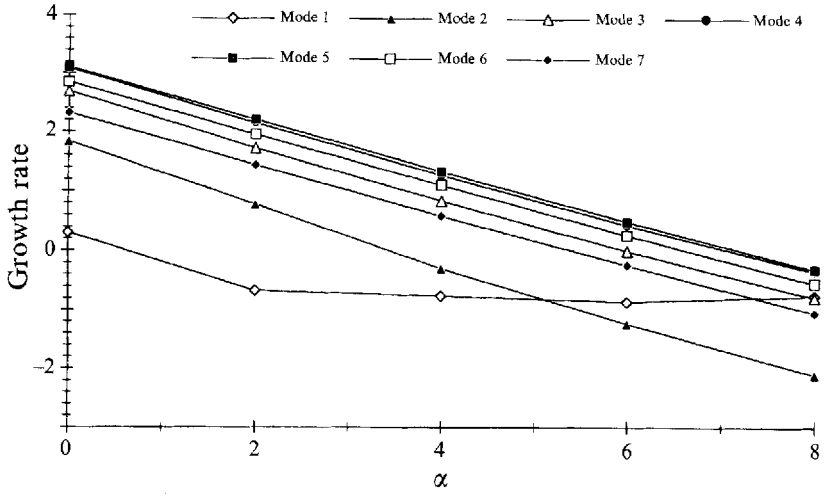

FIGURE 3. Linear initial growth rate as a function of the parameter α (see equation (2.9)) for different azimuthal mode orders. Initial white noise energy varies from 0.1% for mode 1 to 0.0001% for the biggest one. We have kept the following simulations parameters constant: $1/c = 0.1, Ma = 0.18, 1/v = 80, Re = 15, e_s = 0.1, V_I = V_E = 1, M \times N = 64 \times 65$.

the shear radius R_s is 0.022 if the number of Chebyshev polynomials is $N = 129$. The shear width e_s must be somewhat larger than Δr. Consequently, it seems reasonable to set the characteristic shear width at 0.1 in the simulations. The profile will be described by more than four points because, as can be seen on figure 2, the shear is larger than e_s.

As the Rossby number reaches values of the order of 7 in our simulations, the effect of the shear should dominate the effect of the rotation. Note however that the corresponding parameter in the experiments of Nezlin & Snezhkin (1993) can reach 53, and a value of 20 in Chomaz *et al.* (1988). Consequently, our flow is expected to have smaller azimuthal frequencies because m_0 and Ro vary in the same direction.

The value of the friction coefficient α (cf. equation (2.9)) must be chosen according to the experimental characteristics. Its value does not change the nature of the instability because we do not study viscous instability. However if it is too high, it inhibits any instabilities by constraining the velocity profile to remain close to the initial equilibrium one. To give a quantitative account of this effect, the variations of the growth rates (defined at the end of §3.1) of the most unstable modes are represented on figure 3 as a function of α. The bigger the friction force, the smaller the growth rate. Note that in the incompressible case, Chomaz *et al.* (1988) define a friction-based Reynolds number :

$$Re_f = \frac{8\,|\Omega_I - \Omega_E|\,R_s}{e_s\,\alpha}$$

where 60 is the critical value in their computation and 80 in their experiments. These values are consistent with the present compressible case, where $\alpha = 7.25$ gives a critical Re_f value of about 40 at $Ma = 0.18$ and $Re = 15$.

To check if this friction force alone, which is dominant in the experimental set-up, is sufficient to maintain the basic profile, we have removed the shearing force F_s and kept the friction force F_f with two different coefficients. The comparison with the reference case (*a*) where we keep F_s is summarized in table 2.

Run	F_s	α	$\frac{\lvert\overline{u}_\phi\rvert_{max}}{\lvert\overline{u}_\phi\rvert^{(a)}_{max}}$	$\frac{\text{Growth rate}}{\text{Growth rate of } (a)}$	m_0
a	$\neq 0$	2	1	1	2
b	$= 0$	2	0.86	0.3	1
c	$= 0$	10	1.07	0.08	1

TABLE 2. Comparison of three runs with various forcing terms. The following parameters are kept constant: $1/c = 0.7, Ma = 1.4, 1/\nu = 20, Re = 4, e_s = 0.1, \Omega_I = 5(V_I = 1), \Omega_E = 0$, $M \times N = 64 \times 65$. $|\overline{u}_\phi|_{max}$ is the maximum value of the absolute mean tangential velocity $|\overline{u}_\phi(r)|$ when the flow is stationary. Note that the most unstable mode has the order m_0 while the growth rates are given for the same azimuthal mode number of one.

Run	$1/c$	Ma	$1/\nu$	Re	M	N	Time step	Final time
A	0.1	0.18	80	14.5	64	129	5×10^{-5}	60
B	0.7	1.3	20	3.6	64	129	1×10^{-5}	240
C	1.0	1.8	9	1.6	128	129	2×10^{-5}	120

TABLE 3. Characteristic parameters of three different simulations. Other parameters ($e_s = 0.1, V_I = V_E = -1, \alpha = 2$) are kept fixed.

We verify that the 'friction' force alone maintains the profile in its initial shape if the parameter is large enough but then the instability needs a long time to develop (run *c*). Consequently, we will keep the force F_s compensating the viscous damping and the restoring force F_f with usually the intermediate value $\alpha = 2$ (run *a*).

We have explained above the choice of the values of the shear width e_s and of the parameter. Table 3 specifies the other parameters for the three typical runs discussed in the next sections.

Note that the nonlinear flow evolution generates excitation on smaller and smaller scales and as a consequence of the finite spatial resolution, high Mach number simulations require relatively low Reynolds numbers. This resolution constraint explains why steady patterns are presented in this section only for *Ma* not exceeding 2, while linear growth rates may be given for Mach numbers above 20 in the following section.

In all these runs, the geometry is unchanged (see §2) and the rotation period of the inner boundary is about $2\pi/\Omega_I = 1.26$ in non-dimensionalized time units.

The spectral energy for each azimuthal mode m integrated radially gives a global measure of the main features of the flow evolution. The azimuthal power spectrum is thus defined as

$$SPK_{m(t)} = \sum_{n=0}^{N} \left\{ |\hat{u}_\phi(m,n,t)|^2 + |\hat{u}_r(m,n,t)|^2 \right\}, \tag{3.1}$$

where $\hat{f}(m,n,t)$ is the Fourier–Chebyshev component of the function $f(\phi,r,t)$. The growth rate, for a given wavenumber, is proportional to the slope of the power spectrum logarithm as a function of time.

Structures are visualized using density and vorticity contours and velocity vectors.

3.2. *Mach number 0.18 (Run A)*

The time evolution of the energy of the first 10 Fourier modes, for this simulation at weak Mach number, is given in figure 4. The following successive stages are easily identified:

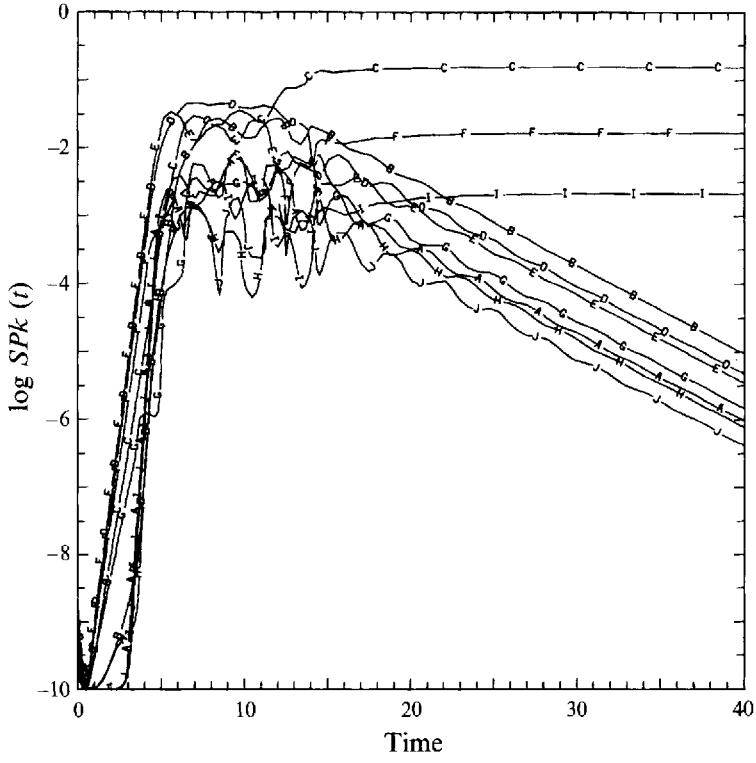

FIGURE 4. Run A. Decimal logarithm of the spectrum defined by equation (3.1) as a function of time t for the first ten orders of the Fourier modes: curve A for $m = 1$, curve B for $m = 2$, curve C for $m = 3, \ldots$, curve J for $m = 10$. The initial white noise energy corresponds to one order below what is given in §2.4. For $0 < t < 20$, there is a point for each time interval 0.5. For $20 < t < 40$, there is a point for each time interval 1.

(i) fast transient (during less than a rotation period) due to the fact that the arbitrary initial conditions are not the eigensolutions of the linearized dynamical equations;

(ii) exponential growth to about $t = 5$ (about 3 rotation periods);

(iii) fluctuations due to non-linear interactions during about ten rotation periods;

(iv) appearance of dominant stationary modes, mode $m = 3$ and its harmonics (labels C, F, I), while the others are decaying quasi-exponentially to at least $t = 60$ (and they are presumed to decay until they reach the numerical round-off level).

The domination of mode $m = 3$ is clearly visible on the density contours at time $t = 40$ (figure 5*a*), with three depressions centred on the shear mean radius at $r = R_s$ (the minimal density is 0.974) separated by smooth density maxima (1.01). Outside the shear mean radius R_s, density maxima along three arms are obtained.

The inner cylinder is rotating in the clockwise direction (retrograde, $\Omega_I < 0$) and the initial vorticity at the shear mean radius R_s has a strong positive maximum ($\nabla \times \boldsymbol{u}|_z = 2\Omega + r\partial\Omega/\partial r = 32$). The vorticity contours at time 40 (figure 5*b*) show a complicated structure with two concentric areas exhibiting a strong radial vorticity variation while the density minima coincide with an enlarged domain of positive vorticity. Negative vorticity appears in between, where density is maximum. Plots of the perturbed velocity fields (figure 5*c*), defined by the difference between the local velocity and the mean azimuthal effective velocity, show also that the density minima

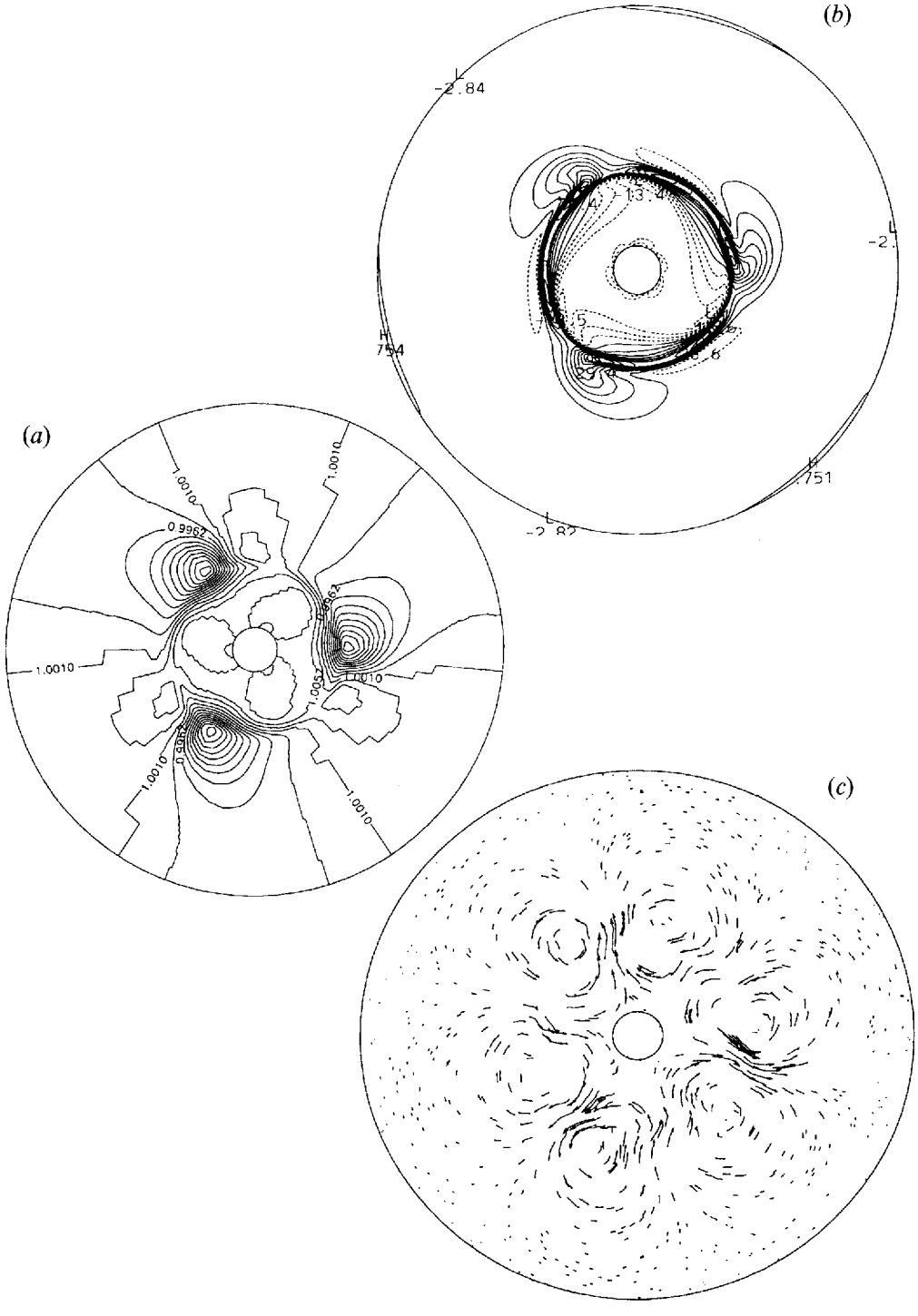

FIGURE 5. Run A at $t = 40$. (*a*) Density isolines: the mean flow and the three vortices move in clockwise direction. (*b*) Velocity curl isolines. (*c*) Perturbed velocity vectors $(u_\phi - \overline{u}_\phi, u_r - \overline{u}_r)_{(\phi,r)}$, where an overbar denotes an average along the tangential direction.

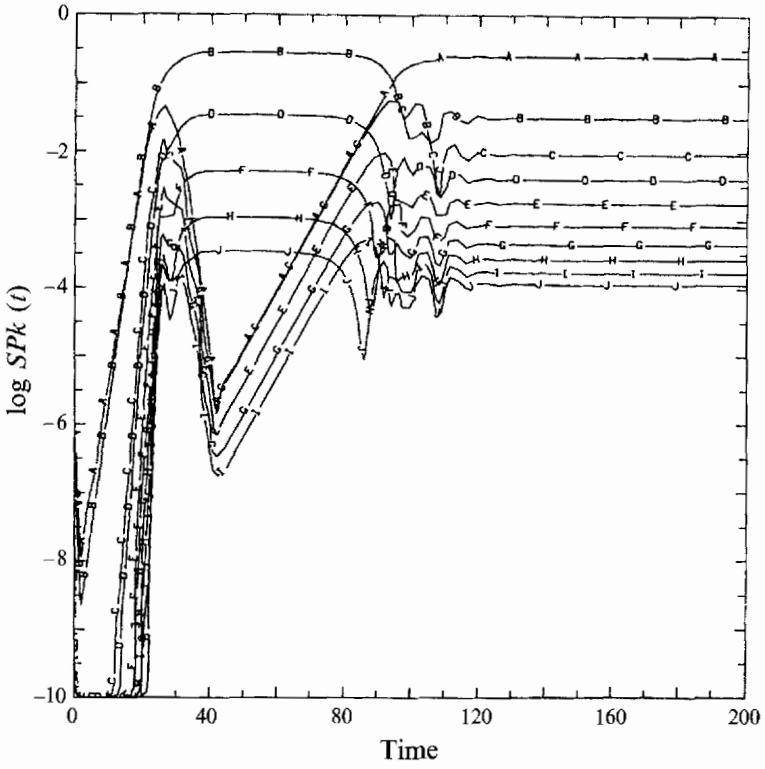

FIGURE 6. Run B. Decimal logarithm of the spectrum defined by equation (3.1) as a function of time t for the first ten orders of the Fourier modes: curve A for $m = 1$, curve B for $m = 2$, curve C for $m = 3, \ldots$, curve J for $m = 10$. Each curve is plotted for time units varying from 2 in increments of 2.

(resp. maxima) coincide with eddies rotating in the anticyclonic (resp. cyclonic) direction. The perturbed flux lines are closed.

The angular velocity of the pattern (Ω_{dr}) is obtained from the temporal evolution at a given point of any flow dynamical variables such as density; then $\Omega_{dr} = -1.57 \pm 0.08$ in non-dimensionnal units. The patterns drift at a speed lower than the mean azimuthal velocity at R_s and they spread beyond this radius where the velocity falls. The convective Mach number based on the real convective velocity of the patterns can be written

$$M_{dr} = \frac{V_{dr} - \Omega_E R_s}{c} \qquad \text{where} \qquad V_{dr} = \Omega_{dr} R_s. \tag{3.2}$$

Then $M_{dr} = 0.130 \pm 01$. We verify that the number of structures decreases either when the Mach number or the shear width increases. Nezlin & Snezhkin (1993) obtained three spirals at a higher Mach number $1.6 < Ma < 2.2$. Their results are compatible with ours if we consider that their ratio e_s/R_s is smaller (local Rossby number 20 compared to 7 in our case).

3.3. *Mach number 1.3 (Run B)*

The evolution of the modal energies of the simulation at transonic Mach number is found to be more complex in the transient phase than before as may be seen on figure 6. The first three stages (cf. run A) extend to about 30 rotation periods and the even modes (label B corresponds to $m = 2$) seem to form a stationary state. However

at $t = 40$, the odd modes suddenly begin to grow exponentially, leading to a steady state dominated by the mode $m = 1$ after $t = 100$.

Figure 7(*a*) shows the density contours at time $t = 54$ when mode 2 is predominant: the density minima are close to the shear mean radius but much lower (0.38) than in run A at low Mach numbers. The same zone also exhibits strong density gradients, but it can be noticed that the density maxima are found at the inner and outer boundaries showing the influence of reflecting boundaries at high Mach numbers (cf. Dolez & Léorat 1991).

It is interesting to compare the qualitative shape of our simulations and the two stable structures of the shallow water experiments figure 8.2 of Nezlin & Snezhkin (1993), although they obtain this configuration at a higher convective Mach number *Ma* of 2.2. The white vortices between grey spirals (recall that the spirals outline elevations in shallow water, i.e. overpressure regions) correspond to our two spread minima of density. Our spirals spread at the outer edge, creating optima, because of reflections, while the experimental set-up avoids reflections.

As in §3.2 above, the minima of density corresponding to a spreading of positive-vorticity regions (figure 7*b*) are separated by negative-vorticity regions still confined to a narrow band.

The most significant result on velocity vectors is given by the pertubed flow (figure 7*c*): the eddies are no longer visible around the density minima and are replaced by two centripetal jets which collide on the external wall, allowing angular momentum transport.

The nature of the instability (see also Nezlin *et al.* 1986) will be discussed but we can already see that the shape of our trailing structures is more spiralled than on figure 5(*a*) at $Ma = 0.18$ because they drift at a higher corresponding Mach number: $\Omega_{dr} = -1.40 \pm 0.08 \Rightarrow V_{dr} = -1.12 \pm 0.07 \Rightarrow M_{dr} = 0.53 \pm 0.05$ (see equation (3.2)).

The transition from $m = 2$ to $m = 1$ is shown on a sequence of density contours (figure 8). The change of mode happens by a kind of shredding interaction after one mode has drifted toward the other. The transition occurs after the mean tangential velocity profile has smoothed. During the transition it broadens again before becoming stationary until the end of integration ($t = 240$). Note that this widening is also observed in the shallow water experiments (see figure 8.6 of Nezlin & Snezhkin 1993).

At dimensionless time 200, the unique structure seems to have retained the memory of the old transition period. The calculation at this time of the pattern drift speed gives $\Omega_{dr} = -1.16 \pm 0.06 \Rightarrow V_{dr} = -0.88 \pm 0.05 \Rightarrow M_{dr} = 0.39 \pm 0.01$. The density contrasts are stronger than in the $m = 2$ regime (the minimum is 0.28 in the shear region and the maximum is 2.4 at the internal boundary) and the perturbed velocity plot is always dominated by a radial jet-like flow.

In this subsection, we have exhibited a transition between two patterns ($m = 2$ then $m = 1$). Indeed, changing *Ma* or e_s by a few tenths of a percent leads to the stabilization of mode 1 or 2 after the initial linear phase.

In view of this transition, the reader might wonder if the three structures of the first run A could collapse into two and then into one stable structure. This is in fact not the case, because:

(i) the total integration time (60) is twelve times the linear growth time in run A (figure 4). Now, the odd modes of run B (figure 6) begin to increase during the nonlinear phase, at $t = 40$, which is only two times the linear growth rate;

(ii) when the odd modes in run B increase, the most energetic one has decreased its energy to the value of 10^{-6}. At $t = 60$, where we stopped the simulation of run A,

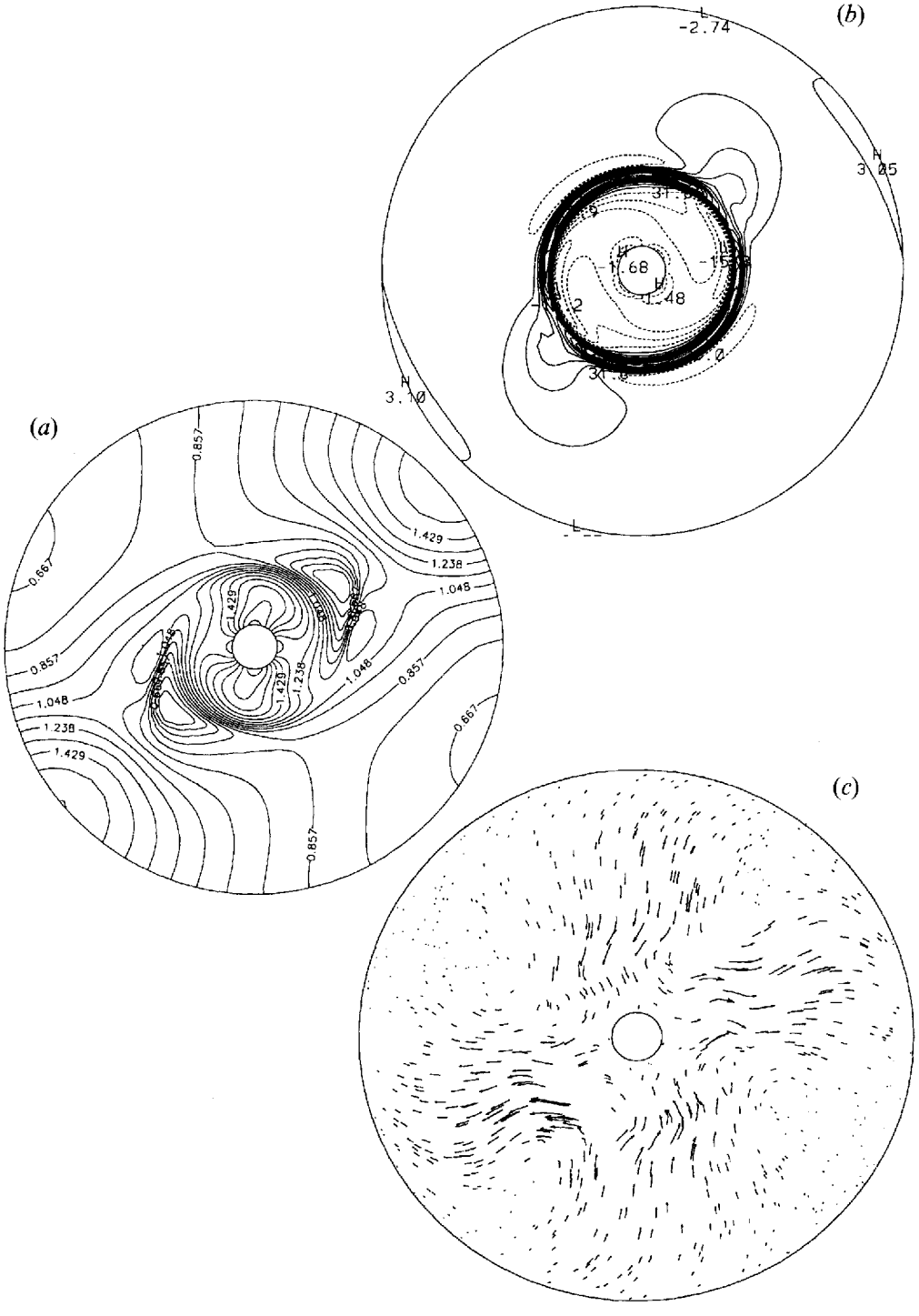

FIGURE 7. Run B at $t = 54$. (*a*) Density isolines: the mean flow and the two vortices move in clockwise direction. (*b*) Velocity curl isolines. (*c*) Perturbed velocity vectors (see caption to figure 5).

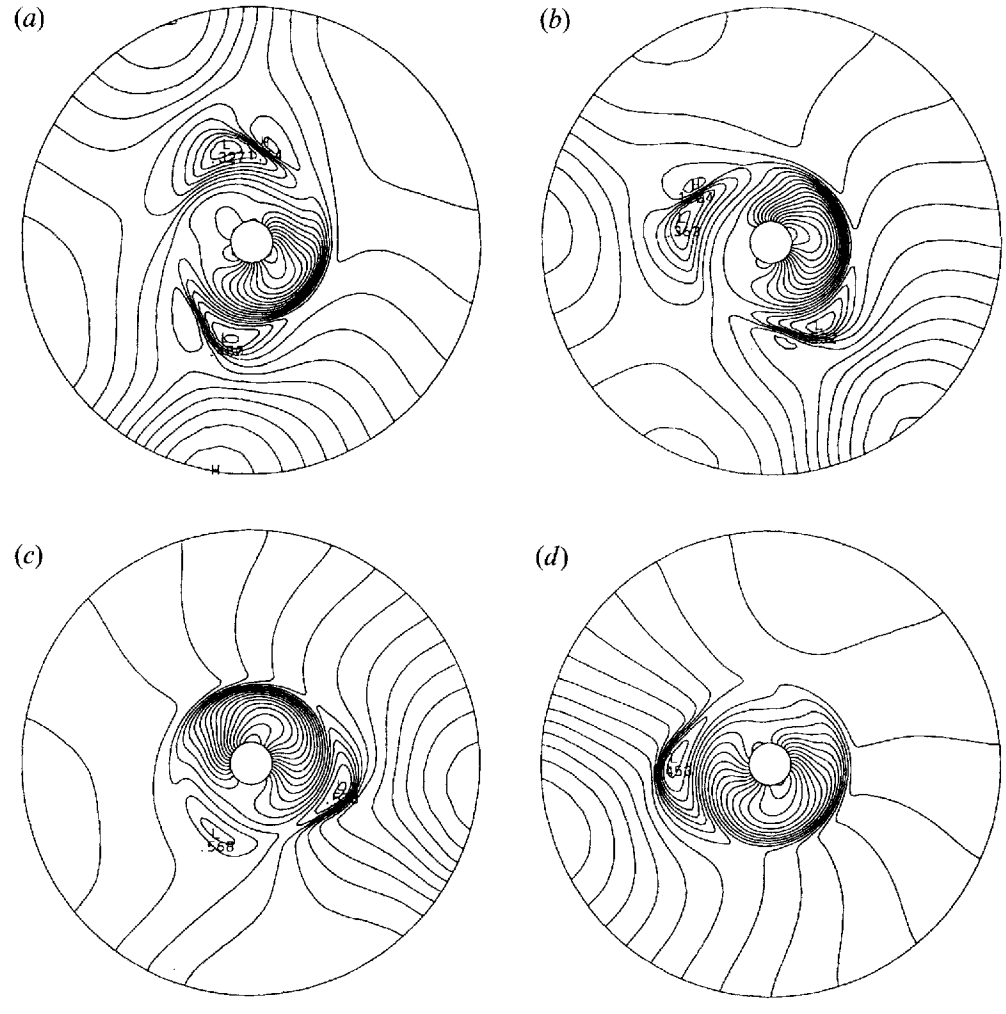

FIGURE 8. Run B. Density isolines at time $t = 90, 94, 98, 100$. Transition between the azimuthal mode $m = 2$ and $m = 1$.

the most energetic of the decaying modes has the equivalent energy of $10^{-7.6}$, which is much lower.

3.4. *Mach number 1.8 (Run C)*

In order to avoid the numerical instabilities associated with the accumulation of energy at the smallest scales, for this simulation at a higher Mach number, we have been compelled to increase the azimuthal resolution to $M = 128$ instead of 64 and to also increase the viscosity ($Re = 1.6$). Thus the characteristic linear growth time is large (figure 9). During the linear phase the mean azimuthal velocity looses only 9% of its initial energy before becoming stationary. The overall results are similar to the preceeding run.

The strongest minimum (0.35) is associated with a maximum density at the outer edge (figure 10*a*), the transition being very thin (strong gradient at the structure edge). The perturbed flow (figure 10*b*) forms two undulating radial jets, one centripetal and one centrifugal.

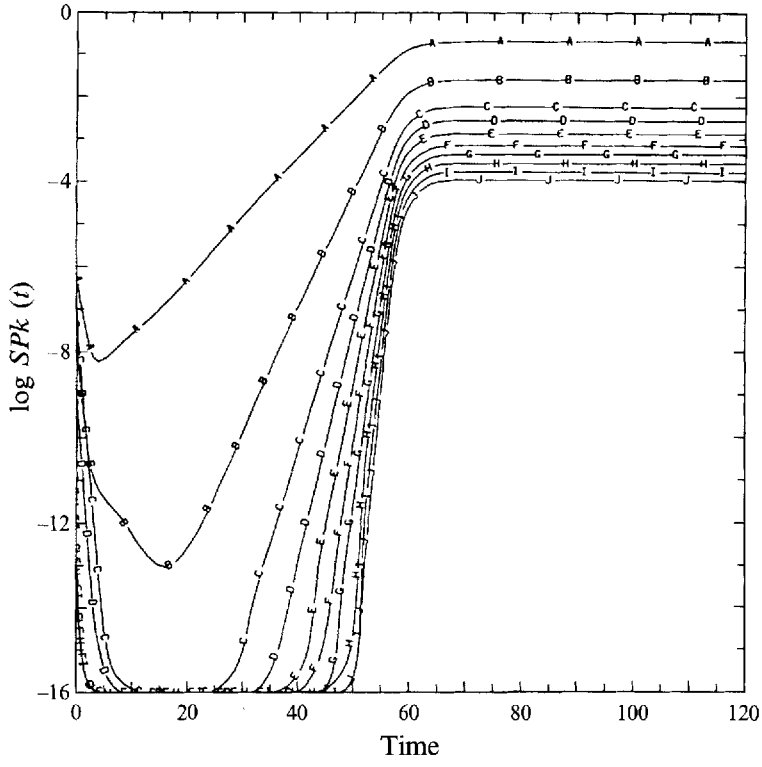

FIGURE 9. Run C. Decimal logarithm of the spectrum defined by equation (3.1) as a function of time t for the first ten orders of the Fourier modes: curve A for $m = 1$, curve B for $m = 2$, curve C for $m = 3, \ldots$, curve J for $m = 10$. Each curve is plotted for time units varying from 2 in increments of 2.

Simulations at higher Mach and Reynolds numbers would be highly instructive to study the possible resonance of turbulent flows but would involve greater numerical resources. The available numerical tools do allow however a more detailed study of the first linear phase of the compressible shear instability which will give more information on its nature.

4. Nature of the instabilities

As already indicated in the introduction, for a given set of flow parameters (geometry of the shear profile, Mach and Reynolds numbers, etc.), two types of terms may be relevant in the dynamical equations to determine the characteristics of the linear instability:

(i) those remaining on taking the limit of infinite curvature radius, which are acting, for example, in the compressible plane mixing layer;

(ii) those present in the centrifugal instability criterion (Morozov 1979): a negative gradient of angular momentum is needed, as well as finite curvature radius and sound speed.

The numerical simulation makes it possible to show the relative contributions of both kinds of physical effects by studying the variation of the linear growth rate when only one parameter is modified. Here we have chosen to vary the Mach number since the compressible mixing layer instability is known to be sensitive to this parameter.

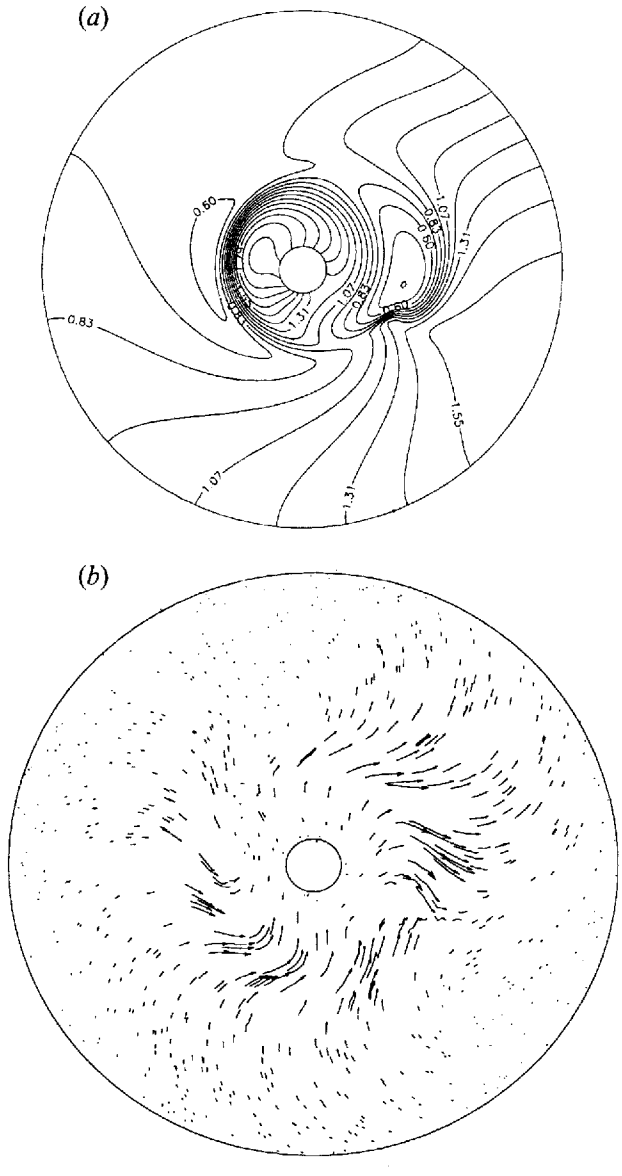

FIGURE 10. Run C at $t = 120$. (*a*) Density isolines: the mean flow and the single vortex move in clockwise direction. (*b*) Perturbed velocity vectors.

To obtain a perfect rectilinear power spectrum slope, we must decrease the white noise energy given as an initial condition in §2.3 by a factor 10. This is achieved in §4.1 when we study the linear growth rates.

4.1. *Variation of the growth rates with the Mach number*

We only deal here with the linear phase of the instability and keep the Reynolds number constant as well as the geometry (inner, shear and outer radius). The boundary velocities, the shear width and the friction force are similar to those used in §3.

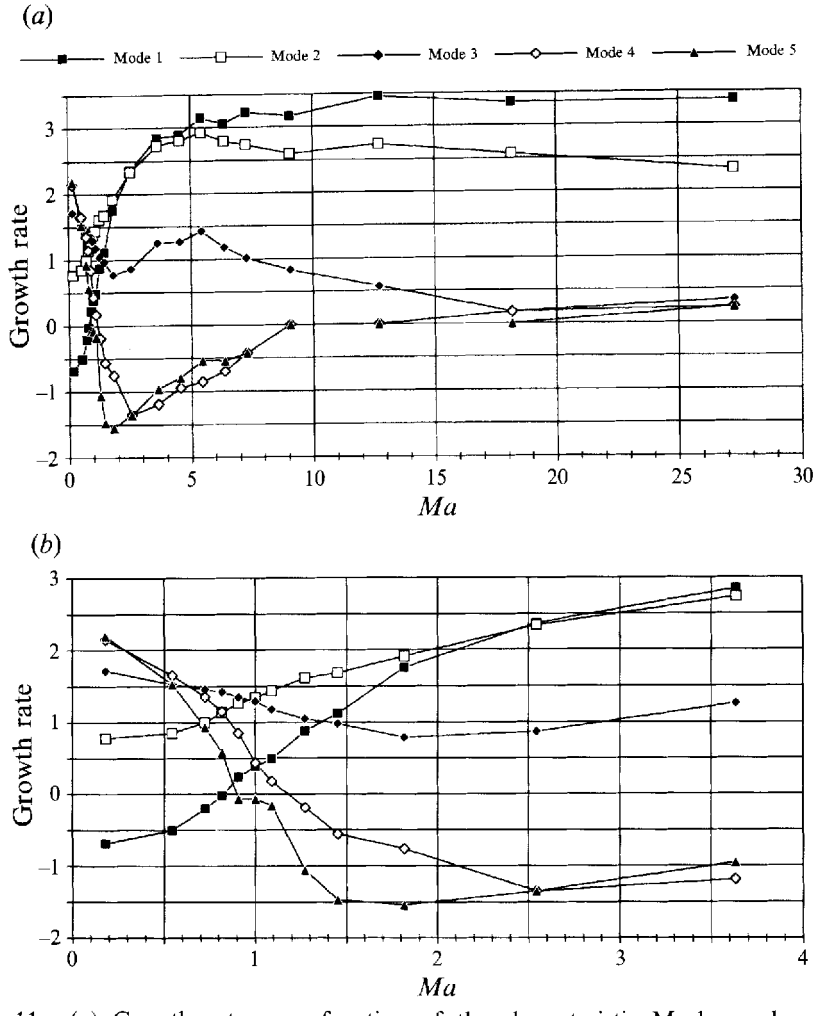

FIGURE 11. (*a*) Growth rate as a function of the characteristic Mach number Ma between 0.18 and 27 for the first five orders of the Fourier modes. The simulations parameters are: $V_I = V_E = -1, 1/v = 80, Re = 14.5, e_s = 0.1, \alpha = 2, M \times N = 64 \times 65$. The uncertainty in the growth rate is about 0.06. (*b*) Enlargement of (*a*) between $0.18 < Ma < 3.6$.

Figure 11 shows the linear growth rates (see §3.1 for the definition) of the five lowest azimuthal modes (still including the most unstable mode) as a function of the characteristic Mach number defined in equation (2.5).

We note first that, as expected, the growth rates vary strongly in the transonic regime and saturate above $Ma = 10$ with the domination of the lowest mode ($m = 1$). Let us examine in more detail the transition around $Ma = 1$ (figure 11*b*):

(i) below $Ma = 2$, the growth rates of all modes except $m = 1$ and $m = 2$ decrease when Ma increases;

(ii) the rank of the most unstable mode decreases when Ma increases: $m_0 = 5$ at $Ma = 0.18$, $m_0 = 4$ at $Ma = 0.28, m_0 = 3$ at $Ma = 0.64, m_0 = 2$ at $Ma = 0.96$ and $m_0 = 1$ at $Ma = 2.4$;

(iii) the growth rates of the two first modes increase with the Mach number.

Observations (i) and (ii) are in agreement with the analysis of the compressible plane shear layer (Blumen *et al.* 1975) and with the experiments on rotating shear

$1/c$	0.1	0.4	0.5
Ma	0.18	0.8	1.0
Growth rate $\Omega_I = 5$, $\Omega_E = 0$	5.38 for $m_0 = 7$	3.19 for $m_0 = 5$ 2.92 for $m = 3$	$> 0\ \forall m$
Growth rate $\Omega_I = 0$, $\Omega_E = 5$	5.35 for $m_0 = 7$	0.13 for $m_0 = 3$	$< 0\ \forall m$

TABLE 4. Initial linear growth rate as a function of the Mach number for two configurations: the first with the angular momentum decreasing outwards, the second with increasing angular momentum with r. The constant parameters are: $e_s = 0.1, 1/\nu = 1000$ that is $Re = 200$, $\alpha = 2$, $M \times N = 64 \times 65$. m_0 is the order of the most unstable mode.

flow; (iii) may be attributed to another instability, say centrifugal instability, favouring the small wavenumbers. In the next subsection, we will try to identify more precisely the centrifugal instability and we will provide evidence of the superposition of the latter instability with the Kelvin–Helmholtz instability at weak Mach numbers.

4.2. *Distinction between the Kelvin–Helmholtz (KH) and the centrifugal instabilities*

Two kinds of simulation are useful for the detection of a centrifugal instability.

First, as the classical linear theory predicts the absence of centrifugal instability when the absolute value of angular momentum ($|\Omega r^2|$) increases with the radius, we have taken $\Omega_I = 0$ and different outer angular velocities Ω_E. We find that an instability develops up to a critical Mach number, with the KH characteristics (decreasing growth rates with increasing Mach numbers). Beyond this Mach number, $Ma_{KH} = 1/c$, the initial flow (local small perturbation superimposed to the the basic flow) is stable, whatever the viscosity (assumed to be greater than the critical viscosity). Ma_{KH} depends on Ω_E: it varies from 0.8 when $\Omega_E = 2$ to 0.4 when $\Omega_E = 10$. Table 4 demonstrates the domination of the KH instability at weak Mach numbers (since the growth rates are close whatever the sign of the angular momentum gradient when $Ma = 0.18$). At supersonic Mach numbers, the centrifugal instability only may exist (positive growth rate when angular momentum decreases outwards) and at transonic Mach numbers both instabilities coexist.

Secondly, to evaluate the impact of the curvature term on the instability, we have removed the centripetal acceleration and the pseudo-gravity F_r from the dynamical equation of the radial velocity. As the Mach number varies, the linear growth rates of the five lowest wavenumbers are given in figure 12. All other parameters are kept identical to those of §4.1 except the external boundary, which is now at rest, so that any centrifugal instability should be relatively favoured.

It can be observed that the growth rates decrease when Ma increases, as before for modes $m > 2$. For all modes, the growth rates remain close to zero above $Ma = 1$ compared to figure 11 (10 times smaller for the mode $m = 1$).

The growth rates obtained cannot be compared to those calculated for the non-stationary modes of the plan-parallel shear layer by Blumen *et al.* (1975) because we have not eliminated all the curvature terms. However, even with no curvature term, they proved, by analytical tools, that the hyperbolic tangent shear layer is unstable to two-dimensional disturbances, at a Mach number above one, through the intermediary of a second mode with growth rate one order of magnitude less than the first mode, responsible for the instability at subsonic Mach number.

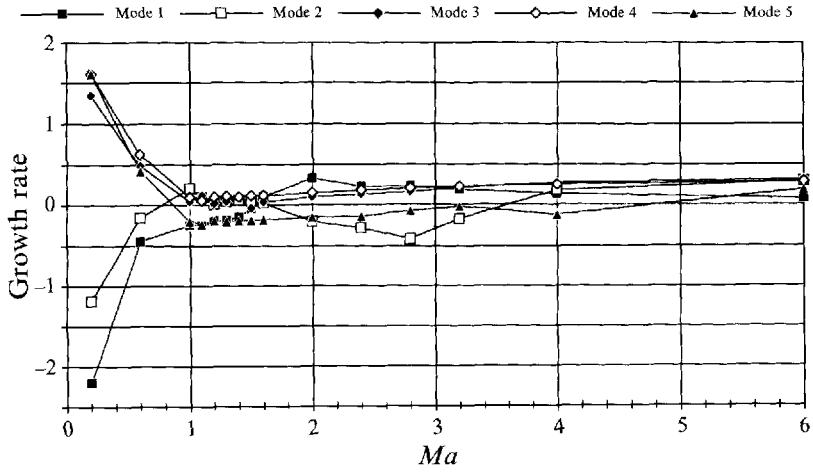

FIGURE 12. Growth rate as a function of the characteristic Mach number Ma for the first five orders of the Fourier modes. We have removed from the dynamical equation the centrifugal force and the force F_r. The other simulations parameters are: $V_I = -1, V_E = 0, 1/v = 80, Re = 16, e_s = 0.1, \alpha = 2, M \times N = 64 \times 65$.

These results are particularly significant and could not be obtained experimentally. They show that two types of instability are encountered in the compressible shear flow:

(i) the KH instability, present whatever the direction of the angular momentum gradient, not affected by the curvature terms, and vanishing at around sonic Mach number;

(ii) the centrifugal instability which needs a negative radial gradient of angular velocity absolute value, centripetal acceleration and a sufficient Mach number to develop.

Chagelishvili, Rogava & Segal (1994) shows a mechanism by which the two-dimensional compressible plane Couette flow is unstable with a linear algebraic growth rate. We did not observe this kind of instability in our simulations, which is natural when some exponential growth exists; but we also did not observe it even in the case of an outward increase of angular momentum absolute value, in supersonic flow, where we had no exponential instability.

It would be interesting to extend the stability analysis of the rotating shear layer beyond the present study by taking into account the possibility of subcritical finite-amplitude instabilities (Dubrulle & Nazarenko 1994). Note that the main feature of our flow is the strong shear imposed at the radius R_s, which makes it very different from a Couette flow.

5. Discussion

5.1. *Comparison with experiments*

To our knowledge, there are no other numerical studies of the nonlinear stability of the rotating shear layer in the transonic regime. It is thus important first to compare the results with those of the experiments and check their reliability before going further in our investigation. The numerical simulations are in agreement with the main experimental results of Nezlin & Snezhkin (1993), despite inescapable differences in the forcing, the boundary conditions and in the Reynolds number: a

localized shear in a subsonic and supersonic rotating flow is the source of instabilities which leads to the formation of rotating structures that are less and less numerous as the Mach number increases. At transonic Mach numbers, trailing spirals (as opposed to leading spirals) form. Their inner tips are situated between depressed vortices, around the radius of strongest shear speed.

In the experiments and in our simulations the vortices drift velocity, compared to the wave velocity, increases with the Mach number and the spirals are wound more tightly as the Mach number increases (cf. figure 8.1 of Nezlin & Snezhkin 1993). This fact is easily understandable if we realize that the vortex emits waves (surface gravity waves in the experiments and sound waves in the numerical simulations). A wake is creating if the vortex moves faster than the wave ($V_{dr}/c > 1$ or $M_{dr} > 1$, see equation (3.2)), in the case of a point source. And if the source has a circular trajectory, the wake looks like a spiral winding more tightly as the source moves faster and which bends backward. For a spread source, like our vortices, wakes are present even with $M_{dr} < 1$.

However, we also observe trailing spirals between vortices during the linear stage of the instability where there are no nonlinear interactions: the vortex would not emit waves. If so, spirals are not generated by vortices during the linear development. In that sense, we agree with the conclusions of Baev, Makov & Fridman (1987), who computed the linearized dynamical equations, stating that:

(i) the spiral-vortex structure has already formed during the linear stage;

(ii) the spiral and vortices are created simultaneously and neither generates the other.

The linear phase of shear instability is only a transition to the interesting phase with nonlinear interactions where we think, together with J. Sommeria (personal discussion), that waves are vortices' wakes.

In the limit of weak Mach numbers, the prevailing instability is of the Kelvin–Helmholtz type. The initial linear growth rates fall with increasing compressibility effects. This instability vanishes at a Mach number depending on the Reynolds number and on the shear profile. This value is to be compared with the theoretical limit of $\sqrt{2}$ for an inviscid vortex sheet flow (Landau 1944).

In the limit of large Mach numbers and with the condition of negative gradient of angular momentum absolute value, the most unstable mode is one-armed and stems from the two-dimensional centrifugal instability. Growth rates are discussed below.

At intermediate Mach numbers both instabilities may occur simultaneously.

Qualitative differences in the spiral shape are observed between numerical and experimental investigations, because:

(i) the smaller ratio R_E/R_s in the numerical study allows less room for the spiral development towards the periphery;

(ii) our numerical spirals are less tightly wound (bigger pitch angle) because the vortices drift at a velocity, compared to the wave speed, much lower than those of the experiment.

The resolution limit in the supersonic regime constrains the numerical Reynolds number to rather small values, which may explain why no turbulent run was obtained. On the other hand, the forced bidimensionalization of the structures does not help the turbulence, essentially three-dimensional, to develop. A turbulent state is achieved in flows with a smooth velocity profile only via three-dimensional perturbations (Orszag & Kells 1980). However, it is not a necessary condition (cf. open flows such as Kolmogorov flow) and we intend to investigate the small scales in order to verify if a realistic turbulent regime can be reach.

The lack of resolution causes quantitative differences too. We are constrained by the width of the shear so that our Rossby number (based on the velocity jump and the shear width, see equation (2.7)) is typically three times smaller than the experimental one of Nezlin & Snezhkin (1993) and of Chomaz *et al.* (1988). As it is known and checked in this paper that the azimuthal wavelength of the instability varies with the shear width, we understand that the order of the most unstable mode is smaller (for the same shear radius) than in the quoted experiments. For example, Snezhkin and Sommeria (personal communication) obtained nine stationary vortices at low inner angular rotation with a Rossby number of 55 (outer annulus at rest), compared to three or four in our simulations with a Rossby number of 7. In order to cope with higher Reynolds number and smaller shear width, a spectral code with two adjacent Chebyshev radial grids seems useful (work currently in progress).

5.2. *Comparison with theoretical predictions*

The experiments cannot give information about the transient linear phase of the instability development. Let us then here compare our results with the local analysis of the centrifugal instability of Morozov (1979), who considers a homogeneous adiabatic non-viscous compressible gas in rotation. He assumed that the instability takes the form of tightly wound spirals for analytical convenience. A discontinuity in the rotation curve led to the first-order instability growth rate $\sigma^{(0)}$ at infinite Reynolds number:

$$\sigma^{(0)} = \frac{(\Omega_I^2 - \Omega_E^2)}{2c} R_s = |\Omega_I + \Omega_E|\, Ma,$$

with $\Omega_I > \Omega_E$. Thus the slope of the growth rate as a function of Ma should be $|\Omega_I + \Omega_E|$. Let us take the evolution of the mode $m = 1$ in the simulations of figure 11(b). Between $Ma = 0.5$ and 2 the growth rate varies linearly with Ma but is influenced by the KH instability ($\sigma \neq 0$ at $Ma = 0$). The slope is 1.8 on the graph compared to $|\Omega_I + \Omega_E| = 5.45$. Note also that the numerical Reynolds number is small ($Re = 14.5$). Moreover, in taking into account a weak blurring in the rotation discontinuity, Morozov corrects the growth rate with the additional negative rate $\sigma^{(1)}$:

$$\sigma^{(1)} = -\frac{e_s}{4c}\left[m^2(\Omega_I - \Omega_E)^2 + \frac{R_s^2}{c^2}(\Omega_I^2 + \Omega_E^2)^2\right]$$

when $Ma < (2R_s/e_s)^{1/2} = 4$. This relation shows that the small orders m are favoured and that large shear widths e_s have stabilizing effects. The maximum of $\sigma = \sigma^{(0)} + \sigma^{(1)} = A_{(m)}Ma - BMa^3$, by taking $\Omega_E = 0$, occurs at $Ma = 1.12$ for the mode $m = 1$ and at $Ma = 1$ for the mode $m = 2$ with our numerical parameters of figure 7 and gives the following growth rates: 3.5 for $m = 1$ and 2.5 for $m = 2$, i.e. closer to but still larger than the numerical ones. The superposition of KH instability in our simulations may be responsible. Notice also the saturation of the growth rates at high Mach numbers while Morozov analytical approximations predicted the extinction of the centrifugal instability at a Mach number close to 2.

Simulations of flows at supersonic velocity represent a challenge. Our simulations at $Ma = 1.8$ show that two obstacles must be overcome in order to obtain useful results: the Reynolds number must be increased and the boundary effects should be minimized. Perhaps both sources of numerical trouble may be cured together.

In the context of the present study, astrophysical disks can be described as supersonic rotating shear layers, where instabilities can be sought as due to the presence of shear, or to the coupling of shear and rotation. However, numerical simulations

alone cannot provide a complete physical explanation of the nature of the instability. In the case of a smooth angular velocity distribution, some approximations have been introduced, and an analysis in terms of over-reflection of waves on a critical layer has been invoked (Goldreich & Lyndell-Bell 1965; Narayan *et al.* 1987). In the situation analysed by Morozov, and in our own simulations, it happens that the instability is directly related to the presence of a strong shear in the flow. It would be useful to know whether some link exists between both instabilities and to derive some instability criterion which can be used in astrophysical situations. In any case it appears that shear and centrifugal instabilities can be responsible for the appearance of large vortices and spiral structures in disks: from there, the density condensations may provide seeds when self-gravity is not negligible (as in protoplanetary disks or in stellar formations in galactic spiralled arms) and the turbulence would contribute efficiently to the transport of angular momentum.

We thank M. Nezlin for inspiring the theme of this study and providing useful critical remarks. We are grateful to J. Sommeria and E. N. Snezhkin for communicating their experimental results and for the stay of M. Tomasini at Lyon.

This work could not have been carried out without the computation time provided by the CCVR (Centre de Calcul Vectoriel pour la Recherche) and by IDRIS (Institut de Développement et des Ressources en Informatique Scientifique).

REFERENCES

ANTIPOV, S. V., NEZLIN, M. V., SNEZHKIN, E. N. & TRUBNIKOV A. S. 1983 Stabilization of a tangential shear instability in shallow water with supersonic fluid flow. *JETP Lett.* **37**, 375.

BAEV, P. V., MAKOV, Y. N. & FRIDMAN, A. M. 1987 Formation of spiral-whirl structure of VK galaxies during the linear stage of hydrodynamic instability. *Sov. Astron. Lett.* **13**, 406.

BAZDENKOV S. V. & POGUTSE O. P. 1983 Supersonic stabilization of a tangential shear in a thin atmosphere. *JETP Lett.* **37**, 378.

BLUMEN, W., DRAZIN, P. G. & BILLINGS, D. F. 1975 Shear layer instability of an inviscid compressible fluid. *J. Fluid Mech.* **71**, 305.

CHAGELISHVILI, G. D., ROGAVA, A. D. & SEGAL, I. N. 1994 Hydrodynamic stability of compressible plane Couette flow. *Phys. Rev.* E **50**, R4283.

CHOMAZ, J. M., RABAUD, M., BASDEVANT, C. & COUDER, Y. 1988 Experimental and numerical investigation of a forced circular shear layer. *J. Fluid Mech.* **187**, 115.

DOLEZ, N. & LÉORAT, J. 1991 Numerical simulations of supersonic plane Couette flow instabilities. In *Turbulence and Coherent Structures* (ed. O. Metais & A. Lesieur). Kluwer.

DUBRULLE, B. & NAZARENKO, S. 1994 On scaling laws for the transition to turbulence in uniform-shear flows. *Europhys. Lett.* **27** , 129.

FRIDMAN, A. M. 1979 Origin of the spiral structure of galaxies. *Sov. Phys. Usp.* **21**, 536.

FRIDMAN, A. M. 1989 In *Dynamics of Astrophysical Disks* (ed. J. A. Sellwood), p. 185 Cambridge University Press.

FRIDMAN, A. M., MOROZOV, A. G., NEZLIN, M. V. & SNEZHKIN, E. N. 1985 Centrifugal instabilities in rotating shallow water and the problem of the spiral structures in Galaxies. *Phys. Lett.* **109A**, 228.

GLATZEL, W. 1987*a* On the stability of compressible differentially rotating cylinders. *Mon. Not. R. Astron. Soc.* **225**, 227.

GLATZEL, W. 1987*b* On the stability of compressible differentially rotating cylinders II. *Mon. Not. R. Astron. Soc.* **228**, 77.

GOLDREICH, P. & LYNDEN-BELL, D. 1965 Spiral arms as sheared gravitational instabilities. *Mon. Not. R. Astron. Soc.* **130**, 125.

LANDAU, L. 1944 Stability of tangential discontinuities in compressible fluid. *Akad. Nauk. SSSR, C. R. (Dokl.)* **44**, 139.

MARCUS, P. S. 1990 Vortex dynamics in a shearing zonal flow. *J. Fluid Mech.* **215**, 393.

MOROZOV, A. G. 1977 Growth of spiral disturbances in the disks of flat galaxies through Kelvin–Helmholtz instability. *Sov. Astron. Lett.* **3**, 103.

MOROZOV, A. G. 1979 Generation of spiral structures in flat galaxies with double peaked rotation curves. *Sov. Astron. Lett.* **23**, 278.

NARAYAN, R., GOLDREICH, P. & GOODMAN, J. 1987 Physics of modes in a differentially rotating system-analysis of the shearing sheet. *Mon. Not. R. Astron. Soc.* **228**, 1.

NEZLIN, M. V., POLIACHENKO, V. L., SNEZHKIN, E. N., TRUBNIKOV, A. S. & FRIDMAN, A. M. 1986 Interarm vortices predicted by laboratory simulations of spiral structures. *Sov. Astron. Lett.* **12**, 213.

NEZLIN, M. V. & SNEZHKIN, E. N. 1993 *Rossby vortices, Spiral structures, Solitons: Astrophysics and Plasma Experiments in Shallow Water Experiments.* Springer.

ORSZAG, S. A. & KELLS, L. C. 1980 Transition to turbulence in plane Poiseuille and plane Couette flow. *J. Fluid Mech.* **96**, 159.

PAPALOIZOU, J. C. B. & PRINGLE, J. E. 1984 The dynamical stability of differentially rotating discs with constant angular momentum. *Mon. Not. R. Astron. Soc.* **208**, 721.

ZASOV A. V. & ZOTOV, V. M. 1989 How often should disk galaxies have double-humped rotation curves? *Sov. Astron. Lett.* **15**, 90.